Robotica (2014) volume 32, pp. 515–532. © Cambridge University Press 2013
doi:10.1017/S0263574713000842

Dynamic modeling and control design for a parallel-mechanism-based meso-milling machine tool

Adam Y. Le*, James K. Mills and Beno Benhabib

Department of Mechanical and Industrial Engineering, 5 King's College Rd, University of Toronto, Toronto, ON M5S 3G8, Canada

(Accepted July 31, 2013. First published online: August 28, 2013)

SUMMARY

A novel rigid-body control design methodology for 6-degree-of-freedom (dof) parallel kinematic mechanisms (PKMs) is proposed. The synchronous control of PKM joints is addressed through a novel formulation of contour and lag errors. Robust performance as a control specification is addressed. A convex combination controller design approach is applied to address the problem of simultaneously satisfying multiple closed-loop specifications. The applied dynamic modeling approach allows the design methodology to be extended to 6-dof spatial PKMs. The methodology is applied to the design of a 6-dof PKM-based meso-milling machine tool and simulations are conducted.

KEYWORDS: Parallel manipulators; Control of robotic systems; Manufacturing; Robot dynamics; Force control.

1. Introduction

In the past decade, meso-scale components (0.5–5.0 mm in size) have found a wide range of applications in areas such as medical, electronics, and the automotive fields. A number of meso-milling machine tools (mMTs) based on serial mechanism have been developed.[1–3] A five-axis desktop mMT design concept based on a 6-degree-of-freedom (dof) spatial parallel kinematic mechanism (PKM) has also been proposed as a solution to the manufacture of complex 3D meso-scale workpieces.[4] PKMs offer higher structural stiffness and lower error accumulation over serial mechanisms. However, the closed-loop linkages of the PKM architecture cause additional dynamic modeling and control challenges.

In rigid-body PKM dynamic modeling, the challenge had been the derivation of explicit dynamic equations using only active joint variables as the set of generalized coordinates. As noted in refs. [5, 6], dynamic equations derived using the Newton–Euler method and the principle of virtual work method have been presented in implicit form. In ref. [7], this challenge was addressed through the application of principle of energy equivalence and the division of the PKM into a set of serial chains with kinematic constraints.[8]

From the dynamics of PKMs, it can be noted that multiple active joint variables must undergo simultaneous motion in order to achieve the desired output motion in task space. Thus, a primary control challenge for PKMs is the synchronization of active joint motions.[9] Synchronous control based on the formulation of a task space contour error was proposed in ref. [10] for machine tool applications. The contour error is defined as the component of the tracking error vector normal to the reference tool path, and its formulation for linear and circular paths was developed in ref. [11]. The contour error in three-axis Cartesian space can be estimated by attaching a moving coordinate frame, known as the Frenet frame, to the reference trajectory.[12] Recent research has focused on improving the estimation of the origin of the Frenet frame, through time delay estimation[13,14] or through geometry.[15]

There is often more than one performance specification under consideration in control design. In order to further improve PKM tracking accuracy, robustness to external disturbances and model

* Corresponding author. E-mail: y.le@mail.utoronto.ca

parameter variations must also be addressed. In ref. [16], a robust performance and stability specification was developed for robotic applications.

The tracking error and robust performance specifications in ref. [16] exhibit the property of convexity.[17,18] A linear control-based design methodology had been proposed in ref. [18] to address the problem of satisfying multiple closed-loop performance specifications simultaneously. The convex combination controller design method is a systematic approach, which solves this control design problem.

For a PKM used in a high-precision mMT, rigid-body gyroscopic forces are induced by high-speed spindle rotor and tool, which can be 200,000 rpm or higher for meso-milling.[19,20] This speed is significantly higher than conventional machining operations and its effect on small desktop-sized high-precision machine tools has yet to be reported in the literature.

In this paper, a novel design methodology is proposed to address the rigid-body control design challenges of PKMs mentioned above. The main contributions of this paper are the development of contour and lag error-based tracking control to address the issue of synchronous control of PKM active joints and the application of the convex combination controller design methodology to address the issue of controller design to satisfy multiple closed-loop performance specifications. Furthermore, with the application of the dynamic modeling method proposed in ref. [7], the design methodology proposed in this paper can be applied to the control design of 6-dof spatial PKMs. The proposed design methodology is demonstrated through its application to the dynamic modeling and control design of a 3-PPRS PKM-based mMT.

The modeling strategy had been applied by the authors for a representative PKM in ref. [21]. This modeling procedure was also applied as a foundation for flexible-body analysis in ref. [22]. The modeling of the spindle gyroscopic forces and the convex combination controller was also discussed by the authors in ref. [23]. In this paper, the main focus is on the development of the design methodology through applications of the aforementioned concepts to address the control design of general 6-dof spatial PKMs. The general case in the modeling of spindle gyroscopic force, where spindle speed is not assumed to be constant, is also considered in this paper. This paper further focuses on the application of convex combination controller for a novel contour error formulation, instead of the Cartesian tracking error.

The paper is organized as follows: Section 2 addresses the dynamic modeling of the PKM. The proposed control design methodology is developed in Section 3. In Section 4, the controller design is applied to a representative PKM-based mMT and simulations are reported. Section 5 concludes the paper.

2. Dynamic Modeling

2.1. System description and inverse kinematics

A representative 3-PPRS PKM configuration for the mMT is shown in Fig. 1. This configuration and its inverse kinematics were presented in ref. [24]. The PKM consists of a fixed circular base of radius r_b on which three active circular prismatic joints, parameterized by angular joint variables θ_i, are mounted at points $\boldsymbol{x}_{Ai}$, for i = 1, 2, 3 denotes the ith chain of the PKM. Three active vertical prismatic joints d_i are placed on the circular prismatic joints. Three passive revolute joints are located at points $\boldsymbol{x}_{Bi}$. Three links, denoted as l_{3i}, of length l_{link}, connect the tool platform through spherical joints at points $\boldsymbol{x}_{Ci}$ to the revolute joints at $\boldsymbol{x}_{Bi}$.

The task space-generalized coordinates are denoted as $\boldsymbol{x}_E = [x \quad y \quad z \quad \alpha \quad \beta \quad \gamma]^T$, where x, y, z denote the tool position in the global coordinate frame $\{\text{O}\}$, and α, β, γ denote the tool orientation based on the *ZYZ* Euler angles convention. Euler angles have been applied to describe the tool platform orientation in refs. [25, 26]. The current frame representation is suitable since γ is always aligned with the machine tool spindle axis, and is considered as a redundant dof in a five-axis machine tool. The tool orientation, then, can be described by α and β. However, when $\beta = 0$, the orientation is singular. In a study of this 3-PPRS PKM, ref. [24] reported additional interior singularities in the hemispherical space, where the inclination angle is between 0° and 30°, as shown in Fig. 1(c). Thus, the workspace of this mechanism is defined such that this portion of the reachable space is avoided.

https://doi.org/10.1017/S0263574713000842 Published online by Cambridge University Press

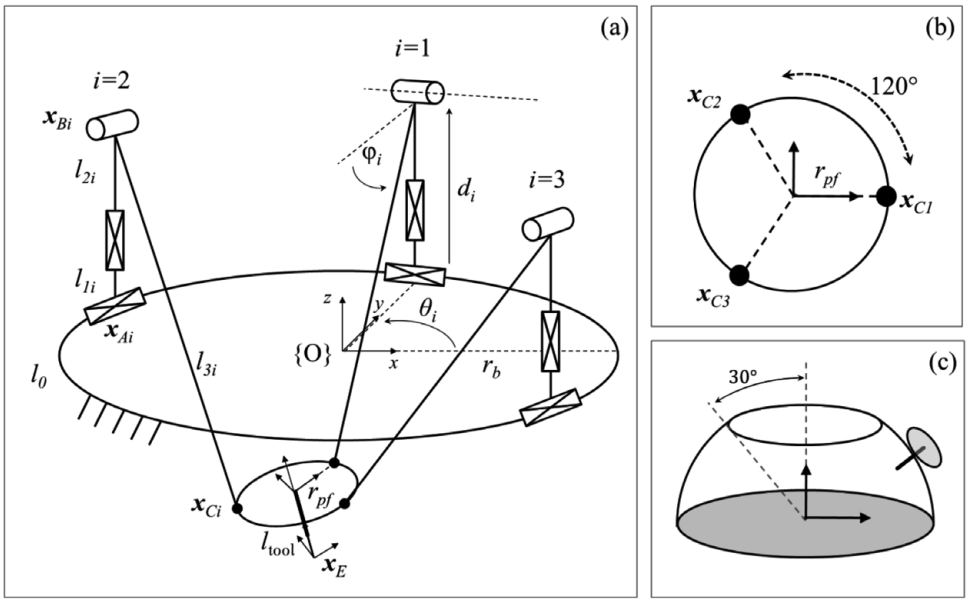

Fig. 1. (a) Representative 3-PPRS PKM configuration; (b) Spherical joint configuration; (c) Workspace.

The vector $\boldsymbol{x}_{Ci} = [x_{Ci} \quad y_{Ci} \quad z_{Ci}]^T$ represents the position of the spherical joints in generalized coordinates, $\boldsymbol{x}_E$, shown in Eq. (1), where $\boldsymbol{R}_{ZYZ}$ is the Euler angle rotation matrix:

$$\begin{cases} \boldsymbol{x}_{C1} = \boldsymbol{R}_{ZYZ} \cdot [r_{pf} \quad 0 \quad l_{\text{tool}}]^T \\ \boldsymbol{x}_{C2} = \boldsymbol{R}_{ZYZ} \cdot \left[\dfrac{-r_{pf}}{2} \quad \dfrac{\sqrt{3} r_{pf}}{2} \quad l_{\text{tool}} \right]^T \\ \boldsymbol{x}_{C3} = \boldsymbol{R}_{ZYZ} \cdot \left[\dfrac{-r_{pf}}{2} \quad \dfrac{-\sqrt{3} r_{pf}}{2} \quad l_{\text{tool}} \right]^T \end{cases}. \tag{1}$$

Above, vector $\boldsymbol{q}_i = [\theta_i \quad d_i \quad \phi_i]^T$ represents the active and passive joint variables in each PKM chain. The inverse kinematic relationships for the active and passive joint variables are

$$\begin{cases} \theta_i = \tan^{-1}\left(\dfrac{y_{Ci}}{x_{Ci}}\right) \\ d_i = z_{Ci} - l_{\text{link}} \cdot \sin(\phi_i) \\ \phi_i = \cos^{-1}\left(\dfrac{r_b - \sqrt{x_{Ci}^2 + y_{Ci}^2}}{l_{\text{link}}}\right) \end{cases}. \tag{2}$$

The active joint space-generalized coordinates are denoted by the vector $\boldsymbol{q}_a = [\theta_1 \quad \theta_2 \quad \theta_3 \quad d_1 \quad d_2 \quad d_3]^T$. The inverse kinematic Jacobian is computed from Eq. (2) analytically. The forward Jacobian matrix $\boldsymbol{J}$ can be computed numerically by inverting $\boldsymbol{J}^{-1}$ or derived analytically. One such method of deriving $\boldsymbol{J}$ analytically is shown in ref. [27]:

$$\begin{cases} \dot{\boldsymbol{q}}_a = J^{-1} \dot{\boldsymbol{x}}_E \\ \dot{\boldsymbol{x}}_E = \boldsymbol{J} \dot{\boldsymbol{q}}_a \end{cases}. \tag{3}$$

2.2. PKM dynamic modeling

The explicit dynamic equations given in Eqs. (4) and (5) are useful for control synthesis since the inertia matrix M, Coriolis and centrifugal force matrix C, and the gravitational force vector $\boldsymbol{g}$ are

https://doi.org/10.1017/S0263574713000842 Published online by Cambridge University Press

isolated from the generalized coordinates in closed form. $\boldsymbol{\tau}_{qa}$ and $\boldsymbol{\tau}_E$ are generalized forces expressed with respect to the generalized coordinates $\boldsymbol{q}_a$ and $\boldsymbol{x}_E$, and the bracketed notation $\boldsymbol{M}(\boldsymbol{q})$ indicates that the matrix $\boldsymbol{M}$ is a function of the generalized coordinates $\boldsymbol{q}$, which can be $\boldsymbol{q}_a$ or $\boldsymbol{x}_E$:

$$\textit{Active joint space} \quad \boldsymbol{\tau}_{qa} = \boldsymbol{M}(\boldsymbol{q}_a)\ddot{\boldsymbol{q}}_a + \boldsymbol{C}(\boldsymbol{q}_a, \dot{\boldsymbol{q}}_a)\dot{\boldsymbol{q}}_a + \boldsymbol{g}(\boldsymbol{q}_a), \tag{4}$$

$$\textit{Taskspace} \quad \boldsymbol{\tau}_E = \boldsymbol{M}(\boldsymbol{x}_E)\ddot{\boldsymbol{x}}_E + \boldsymbol{C}(\boldsymbol{x}_E, \dot{\boldsymbol{x}}_E)\dot{\boldsymbol{x}}_E + \boldsymbol{g}(\boldsymbol{x}_E). \tag{5}$$

The methodology developed in ref. [7] is applied to derive the PKM dynamic model. Using the principle of energy equivalence,[8] the PKM is sub-divided into the following components: the tool platform, the actuator chain (which includes actuators components described by θ_i and d_i), and the three links l_{3i}. The kinetic energy T and potential energy U are determined for each component and the Lagrangian formulation, in Eq. (6), is applied to obtain the generalized forces $\boldsymbol{\tau}$ of each component, shown in Eqs. (7)–(9).

The generalized forces for the components are derived using different generalized coordinates. The dynamics of the actuator chains $\boldsymbol{\tau}_{\text{act}}$ is derived with respect to $\boldsymbol{q}_a$. The dynamics of the tool platform $\boldsymbol{\tau}_{pf}$ is derived with respect to $\boldsymbol{x}_E$. The dynamics of the links $\boldsymbol{\tau}_{\text{link}}$ is derived with respect to $\boldsymbol{q}_i$:

$$\boldsymbol{\tau} = \frac{d}{dt}\left(\frac{\partial T}{\partial \dot{\boldsymbol{q}}}\right) - \frac{\partial T}{\partial \boldsymbol{q}} + \frac{\partial U}{\partial \boldsymbol{q}}, \tag{6}$$

$$\textit{Actuator chains} \quad \boldsymbol{\tau}_{\text{act}} = \boldsymbol{M}_{\text{act}}\ddot{\boldsymbol{q}}_a + \boldsymbol{C}_{\text{act}}\dot{\boldsymbol{q}}_a + \boldsymbol{g}_{qa}, \tag{7}$$

$$\textit{Tool platform} \quad \boldsymbol{\tau}_{pf} = \boldsymbol{M}_{pf}\ddot{\boldsymbol{x}}_E + \boldsymbol{C}_{pf}\dot{\boldsymbol{x}}_E + \boldsymbol{g}_{pf}, \tag{8}$$

$$\textit{Links } l_{3i} \quad \boldsymbol{\tau}_{\text{link}} = \boldsymbol{M}_{\text{link}}\ddot{\boldsymbol{q}}_i + \boldsymbol{C}_{\text{link}}\dot{\boldsymbol{q}}_i + \boldsymbol{g}_{\text{link}}. \tag{9}$$

The mass matrices $\boldsymbol{M}$ are obtained by differentiating $\boldsymbol{\tau}$ with respect to $\ddot{\boldsymbol{q}}$. The gravitational force g is derived from $\partial U/\partial \boldsymbol{q}$. The kinetic energy is, then, redefined as

$$T = \frac{1}{2}\dot{\boldsymbol{q}}^T \boldsymbol{M}\dot{\boldsymbol{q}}. \tag{10}$$

By re-applying the Lagrangian formulation to T, matrix C is obtained from terms multiplied by $\dot{\boldsymbol{q}}$.[28]

Coordinate transformations are required to express Eqs. (7)–(9) in a single set of generalized coordinates, either $\boldsymbol{q}_a$ or $\boldsymbol{x}_E$. Only then the generalized forces of the components can be combined to form the complete PKM generalized forces. In this paper, only the general steps are presented, with details of coordinate transformations presented in refs. [7, 21]. For the three links l_{3i}, a coordinate transformation from $\boldsymbol{\tau}_{\text{link}}(\boldsymbol{q}_i)$ to $\boldsymbol{\tau}_{\text{link}}(\boldsymbol{x}_e)$ is required. The generalized forces of the links l_{3i} and the platform, now both expressed in terms of $\boldsymbol{x}_e$, are summed together as

$$\boldsymbol{\tau}_{pf\_\text{link}}(\boldsymbol{x}_e) = \boldsymbol{\tau}_{pf}(\boldsymbol{x}_e) + \boldsymbol{\tau}_{\text{link}}(\boldsymbol{x}_e). \tag{11}$$

A similar coordinate transformation is performed to express $\boldsymbol{\tau}_{pf\_\text{link}}(\boldsymbol{x}_e)$ in active joint coordinates $\boldsymbol{q}_a$ using the inverse Jacobian $\boldsymbol{J}^{-1}$ from Eq. (3):

$$\tau_{pf\_\text{link}}(\boldsymbol{x}_e) \rightarrow \boldsymbol{\tau}_{pf\_\text{link}}(\boldsymbol{q}_a). \tag{12}$$

Finally, the PKM dynamic equation is the sum of the components:

$$\boldsymbol{\tau}_{PKM}(\boldsymbol{q}_a) = \boldsymbol{\tau}_{pf\_\text{link}}(\boldsymbol{q}_a) + \boldsymbol{\tau}_{\text{act}}(\boldsymbol{q}_a). \tag{13}$$

2.3. Dynamic modeling of rigid spindle gyroscopic forces

Rigid-body gyroscopic forces arise when a spinning object is rotated along an axis normal to the spinning axis and is induced on the axis binormal to the two axes that are undergoing rotation. In

https://doi.org/10.1017/S0263574713000842 Published online by Cambridge University Press

order to model this phenomenon for a tool rotor assembly attached to a PKM, the dynamics of the rotor assembly is treated as a serial component. The rotation of the rotor assembly, defined by the variable ξ, is considered as an additional dof, which lies on the same axis as γ.

The axes of rotation for γ and ξ are the same, such that a new variable ζ is formed as

$$\zeta = \gamma + \xi. \tag{14}$$

A new task space-generalized coordinate using ζ is defined as

$$\tilde{\boldsymbol{x}}_\zeta = [x \quad y \quad z \quad \alpha \quad \beta \quad \zeta]^T. \tag{15}$$

The kinetic energy of the rotor assembly is

$$T_{sp} = \frac{1}{2} m_{sp} \dot{\boldsymbol{x}}_{sp}{}^T \dot{\boldsymbol{x}}_{sp} + \frac{1}{2} \boldsymbol{\omega}_{sp}{}^T \boldsymbol{R}^T \boldsymbol{I}_{sp} \boldsymbol{R} \boldsymbol{\omega}_{sp}. \tag{16}$$

The translational velocity of the rotor assembly is

$$\dot{\boldsymbol{x}}_{sp} = \frac{d}{dt} \left([x \quad y \quad z]^T + \boldsymbol{R} \left[0 \quad 0 \quad {}^{l_{\text{tool}}}\!/_2 \right]^T \right). \tag{17}$$

The expression $\boldsymbol{R}[0 \quad 0 \quad l_{\text{tool}}/2]^T$ is a function of (α, β) only. The angular velocity is

$$\boldsymbol{\omega}_{sp} = \mathcal{H} [\dot{\alpha} \quad \dot{\beta} \quad \dot{\zeta}]^T, \tag{18}$$

where $\mathcal{H}$ relates angular velocities to the derivatives of Euler angles[28] and is expressed as

$$\mathcal{H} = \begin{bmatrix} 0 & -\sin\alpha & \cos\alpha \sin\beta \\ 0 & \cos\alpha & \sin\alpha \sin\beta \\ 1 & 0 & \cos\beta \end{bmatrix}. \tag{19}$$

The inertia tensor $\boldsymbol{I}_{sp} = \text{diag}[I_{xx} \quad I_{yy} \quad I_{zz}]$ is defined in the local frame, assuming that the rotor is symmetric about its rotational axis:

$$I_{xx} = I_{yy}. \tag{20}$$

The potential energy of the rotor assembly is

$$U_{sp} = -m_{sp} (\boldsymbol{x}_{sp})_z. \tag{21}$$

Applying the Lagrangian formulation, the rotor dynamic equation is

$$\boldsymbol{\tau}_\zeta = \boldsymbol{M}_\zeta (\tilde{\boldsymbol{x}}_\zeta) \ddot{\tilde{\boldsymbol{x}}}_\zeta + \boldsymbol{C}_\zeta (\dot{\tilde{\boldsymbol{x}}}_\zeta, \tilde{\boldsymbol{x}}_\zeta) \dot{\tilde{\boldsymbol{x}}}_\zeta + \boldsymbol{g}_\zeta. \tag{22}$$

Neither the mass matrix $\boldsymbol{M}_\zeta(\tilde{\boldsymbol{x}}_\zeta)$ nor the gravity force vector $\boldsymbol{g}_\zeta$ is a function of ζ, when $I_{xx} = I_{yy}$. Matrix $\boldsymbol{C}_\zeta(\dot{\tilde{\boldsymbol{x}}}_\zeta, \tilde{\boldsymbol{x}}_\zeta)$ is given in Eq. (23), where * are terms unrelated to $\dot{\zeta}$:

$$\boldsymbol{C}_\zeta (\dot{\tilde{\boldsymbol{x}}}_\zeta, \tilde{\boldsymbol{x}}_\zeta) = \begin{bmatrix} 0 & 0 & 0 & * & * & 0 \\ 0 & 0 & 0 & * & * & 0 \\ 0 & 0 & 0 & 0 & * & 0 \\ 0 & 0 & 0 & * & * - \frac{I_{zz} \dot{\zeta} \sin\beta}{2} & -\frac{I_{zz} \dot{\beta} \sin\beta}{2} \\ 0 & 0 & 0 & * + \frac{I_{zz} \dot{\zeta} \sin\beta}{2} & 0 & -\frac{I_{zz} \dot{\alpha} \sin\beta}{2} \\ 0 & 0 & 0 & * & * & 0 \end{bmatrix}, \tag{23}$$

https://doi.org/10.1017/S0263574713000842 Published online by Cambridge University Press

where $\boldsymbol{C}_\zeta(\dot{\tilde{\boldsymbol{x}}}_\zeta, \tilde{\boldsymbol{x}}_\zeta)$ is a function of $\dot{\zeta}$ in four elements C_{45}, C_{46}, C_{54} and C_{56}, and not a function of ζ. The relevant gyroscopic terms in vector $\boldsymbol{C}_\zeta(\dot{\tilde{\boldsymbol{x}}}_\zeta, \tilde{\boldsymbol{x}}_\zeta)\dot{\tilde{\boldsymbol{x}}}_\zeta$ are

$$\begin{cases} (\tau_{\text{gyro}})_a = -I_{zz}\dot{\zeta}\dot{\beta}\sin\beta = -I_{zz}\dot{\gamma}\dot{\beta}\sin\beta - I_{zz}\dot{\xi}\dot{\beta}\sin\beta \\ (\tau_{\text{gyro}})_b = I_{zz}\dot{\zeta}\dot{\alpha}\sin\beta = I_{zz}\dot{\gamma}\dot{\alpha}\sin\beta + I_{zz}\dot{\xi}\dot{\alpha}\sin\beta \end{cases}, \tag{24}$$

where $(\tau_{\text{gyro}})_a$ is the gyroscopic moment about the z axis contributed by the angular velocity $\dot{b}$ and spindle velocity $\dot{\zeta}$. $(\tau_{\text{gyro}})_b$ is the gyroscopic moment about the current y axis following the Euler angles convention. The vector $\boldsymbol{C}_\zeta(\dot{\tilde{\boldsymbol{x}}}_\zeta, \tilde{\boldsymbol{x}}_\zeta)\dot{\tilde{\boldsymbol{x}}}_\zeta$ is separated into two terms: $\boldsymbol{C}(\boldsymbol{x}_E, \dot{\boldsymbol{x}}_E)\dot{\boldsymbol{x}}_E$ and $\boldsymbol{C}_{\text{gyro}}(\dot{\alpha}, \dot{\beta}, \dot{\xi})\dot{\boldsymbol{x}}_\xi$, the latter of which contains only the gyroscopic terms. The vector $\dot{\boldsymbol{x}}_\xi$ is defined as

$$\dot{\boldsymbol{x}}_\xi = [0 \quad 0 \quad 0 \quad \dot{\alpha} \quad \dot{\beta} \quad \dot{\xi}]^T. \tag{25}$$

There are also gyroscopic terms in matrix $\boldsymbol{M}_{sp\zeta}(\tilde{\boldsymbol{x}}_\zeta)\ddot{\tilde{\boldsymbol{x}}}_\zeta$. The gyroscopic moments are found in the fourth and sixth row:

$$\boldsymbol{M}_{sp\zeta}(\tilde{\boldsymbol{x}}_\zeta)\ddot{\tilde{\boldsymbol{x}}}_\zeta = \begin{bmatrix} * & 0 & 0 & * & * & 0 \\ 0 & * & 0 & * & * & 0 \\ 0 & 0 & * & 0 & * & 0 \\ * & * & 0 & * & 0 & (I_{zz})_{sp}\cos\beta \\ * & * & * & 0 & * & 0 \\ 0 & * & * & * & 0 & (I_{zz})_{sp} \end{bmatrix} \begin{bmatrix} \ddot{x} \\ \ddot{y} \\ \ddot{z} \\ \ddot{\alpha} \\ \ddot{\beta} \\ \ddot{\zeta} \end{bmatrix} = \begin{bmatrix} * \\ * \\ * \\ * + \ddot{\zeta}(I_{zz})_{sp}\cos\beta \\ * \\ * + \ddot{\zeta}(I_{zz})_{sp} \end{bmatrix}. \tag{26}$$

The vector $\boldsymbol{M}_{sp\zeta}(\tilde{\boldsymbol{x}}_\zeta)\ddot{\tilde{\boldsymbol{x}}}_\zeta$ is also separated into two terms: $\boldsymbol{M}_{sp}(\boldsymbol{x}_E)\ddot{\boldsymbol{x}}_E$ and the gyroscopic term $\boldsymbol{M}_{\text{gyro}}(\beta)\ddot{\boldsymbol{x}}_\xi$. In this case, Eq. (22) is rewritten to isolate the gyroscopic forces:

$$\boldsymbol{M}_{sp}(\boldsymbol{x}_E)\ddot{\boldsymbol{x}}_E + \boldsymbol{C}_{sp}(\boldsymbol{x}_E, \dot{\boldsymbol{x}}_E)\dot{\boldsymbol{x}}_E + \boldsymbol{g}_{sp}(\boldsymbol{x}_E) + [\boldsymbol{M}_{\text{gyro}}(\beta)\ddot{\boldsymbol{x}}_\xi + \boldsymbol{C}_{\text{gyro}}(\dot{\alpha}, \dot{\beta}, \dot{\xi})\dot{\boldsymbol{x}}_\xi] = \tau_{sp}. \tag{27}$$

In the special case, where the rotor velocity $\dot{\xi}$ is constant, such that $\ddot{\xi} = 0$, and $\ddot{\zeta} = \ddot{\gamma}$, $\boldsymbol{M}_{\text{gyro}}(\beta)\ddot{\boldsymbol{x}}_\xi = 0$.

3. Control Design

3.1. Contour and lag error formulation using circular approximation

The challenge of synchronous control is addressed through the development of a novel contour error estimation method based on a circular approximation of reference trajectory. In order to effectively apply the approximation, the tracking errors must be small compared to the instantaneous radius of the tool path,[14] which is defined as the inverse of the curvature, or the radius of curvature.[29] Given reference trajectory $\boldsymbol{x}_{\text{ref}}, \dot{\boldsymbol{x}}_{\text{ref}}, \ddot{\boldsymbol{x}}_{\text{ref}}$, the Frenet frame is defined as

$$\boldsymbol{F} = [\hat{\boldsymbol{t}} \quad \hat{\boldsymbol{n}} \quad \hat{\boldsymbol{b}}], \tag{28}$$

where

$$\begin{cases} \hat{\boldsymbol{t}} = \frac{\dot{\boldsymbol{x}}_{\text{ref}}}{\|\dot{\boldsymbol{x}}_{\text{ref}}\|} \\ \hat{\boldsymbol{n}} = \frac{\dot{\boldsymbol{x}}_{\text{ref}} \times (\ddot{\boldsymbol{x}}_{\text{ref}} \times \dot{\boldsymbol{x}}_{\text{ref}})}{\|\dot{\boldsymbol{x}}_{\text{ref}}\| \|\ddot{\boldsymbol{x}}_{\text{ref}} \times \dot{\boldsymbol{x}}_{\text{ref}}\|} \\ \hat{\boldsymbol{b}} = \hat{\boldsymbol{t}} \times \hat{\boldsymbol{n}} \end{cases}, \tag{29}$$

and $\hat{\boldsymbol{t}}$ is the unit vector tangential to $\boldsymbol{x}_{\text{ref}}$ and $\hat{\boldsymbol{n}}$ and $\hat{\boldsymbol{b}}$ are unit vectors normal to $\boldsymbol{x}_{\text{ref}}$.

Under the small tracking error assumption, the sections of the tool path adjacent to the current reference point, denoted as $\boldsymbol{x}_{\text{ref}}(t_o)$, are approximated by a circle having the same radius as the radius of curvature at $\boldsymbol{x}_{\text{ref}}(t_o)$, denoted as ρ_{circ}, and one that lies on the plane defined by $\hat{\boldsymbol{t}}$ and $\hat{\boldsymbol{n}}$ as shown

https://doi.org/10.1017/S0263574713000842 Published online by Cambridge University Press

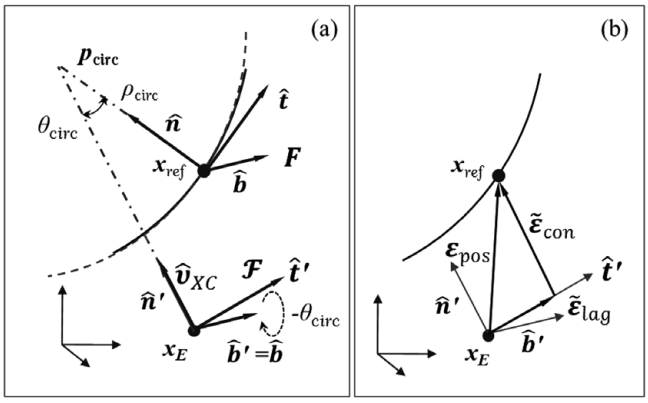

Fig. 2. (a) Spatial circular approximation of contour error; (b) Contour and lag error.

in Fig. 2. ρ_{circ} is calculated as

$$\rho_{\text{circ}} = \frac{\|\dot{\boldsymbol{x}}_{\text{ref}}\|^3}{\|\dot{\boldsymbol{x}}_{\text{ref}} \times \ddot{\boldsymbol{x}}_{\text{ref}}\|}, \quad \text{for } \dot{\boldsymbol{x}}_{\text{ref}} \neq 0. \tag{30}$$

The center point of the circle, denoted as $\boldsymbol{p}_{\text{circ}}$, in Cartesian frame is

$$\boldsymbol{p}_{\text{circ}} = [\boldsymbol{p}_x \quad \boldsymbol{p}_y \quad \boldsymbol{p}_z]^T = \boldsymbol{x}_{\text{ref}}(t_o) + \rho_{\text{circ}} \cdot \hat{\boldsymbol{n}}. \tag{31}$$

A new unit vector $\hat{v}_{XC}$ is defined as

$$\hat{\boldsymbol{v}}_{XC} = \frac{\boldsymbol{p}_{\text{circ}} - \boldsymbol{x}_E}{\|\boldsymbol{p}_{\text{circ}} - \boldsymbol{x}_E\|}, \tag{32}$$

where $\hat{\boldsymbol{v}}_{XC}$ does not lie on the same plane defined by $\hat{\boldsymbol{t}}$ and $\hat{\boldsymbol{n}}$, since the tool position $\boldsymbol{x}_E$ can be at any arbitrary location about $\boldsymbol{x}_{\text{ref}}$. Since $\hat{\boldsymbol{v}}_{XC}$ passes through $\boldsymbol{p}_{\text{circ}}$, a projection of $\hat{\boldsymbol{v}}_{XC}$ on the $\hat{\boldsymbol{t}}\hat{\boldsymbol{n}}$ plane is normal to the circle. If ρ_{circ} is much greater than the tracking error, it is assumed that the projection of $\hat{\boldsymbol{v}}_{XC}$ on the $\hat{\boldsymbol{t}}\hat{\boldsymbol{n}}$ plane is approximately equal to $\hat{\boldsymbol{v}}_{XC}$.

The angle between $\hat{\boldsymbol{v}}_{XC}$and $\hat{\boldsymbol{n}}$, denoted as θ_{circ}, is calculated as

$$\theta_{\text{circ}} = \cos^{-1}(\hat{\boldsymbol{v}}_{XC} \cdot \hat{\boldsymbol{n}}). \tag{33}$$

In order to form an accurate contour error estimation, the Frenet frame $\boldsymbol{F}$ is rotated about $\hat{\boldsymbol{b}}$ by $\boldsymbol{R}_{\theta_{\text{circ}}}$, such that the new $\hat{\boldsymbol{n}}'$ will be approximately aligned with $\hat{\boldsymbol{v}}_{XC}$:

$$\boldsymbol{R}_{\theta_{\text{circ}}} = \begin{bmatrix} \cos(-\theta_{\text{circ}}) & -\sin(-\theta_{\text{circ}}) & 0 \\ \sin(-\theta_{\text{circ}}) & \cos(-\theta_{\text{circ}}) & 0 \\ 0 & 0 & 1 \end{bmatrix} \tag{34}$$

The new Frenet frame $\boldsymbol{\mathcal{F}}$ is

$$\boldsymbol{\mathcal{F}} = \boldsymbol{F}\boldsymbol{R}_{\theta_{\text{circ}}} = \begin{bmatrix} \hat{\boldsymbol{t}}' & \hat{\boldsymbol{n}}' & \hat{\boldsymbol{b}}' \end{bmatrix}. \tag{35}$$

Equation (35) establishes a relationship between tracking error $\boldsymbol{e}$ in the global coordinate frame and the tracking error ε defined in the new moving coordinate frame:

$$\boldsymbol{e} = \boldsymbol{\mathcal{F}}\boldsymbol{\varepsilon} \leftrightarrow \boldsymbol{\varepsilon} = \boldsymbol{\mathcal{F}}^T\boldsymbol{e} = [\,\varepsilon_t \quad \varepsilon_n \quad \varepsilon_b\,]^T. \tag{36}$$

https://doi.org/10.1017/S0263574713000842 Published online by Cambridge University Press

The contour error $\boldsymbol{\varepsilon}_{\text{con}}$ and lag error $\boldsymbol{\varepsilon}_{\text{lag}}$ are defined by $\boldsymbol{\varepsilon}$ as

$$\begin{cases} \|\boldsymbol{\varepsilon}_{\text{con}}\| = \sqrt{\varepsilon_n^2 + \varepsilon_b^2} \\ \|\boldsymbol{\varepsilon}_{\text{lag}}\| = \|\varepsilon_t\| \end{cases}. \tag{37}$$

In the proposed control design, the minimization of contour error is more important than minimization lag error as the contour error represents the normal deviation away from the reference trajectory.

3.2. Control law

The proposed control strategy comprises two components: feedback linearization and contour and lag error linear control. The feedback linearization methodology is well developed.[30] The rigid-body task space dynamics of a real PKM system is defined as

$$\tilde{\boldsymbol{M}}\ddot{\boldsymbol{x}}_E + \tilde{\boldsymbol{C}}\dot{\boldsymbol{x}}_E + \tilde{\boldsymbol{g}} + \tilde{\boldsymbol{\tau}}_C + \boldsymbol{\tau}_\Delta = \boldsymbol{\tau}_{X_E}, \tag{38}$$

where $\boldsymbol{\tau}_C$ are additional forces that are to be compensated, such as the gyroscopic forces and cutting forces. $\boldsymbol{\tau}_\Delta$ is the un-modeled disturbance. $\tilde{\boldsymbol{M}}$, $\tilde{\boldsymbol{C}}$, $\tilde{\boldsymbol{g}}$, and $\tilde{\boldsymbol{\tau}}_C$ are the real system parameters, which are defined by $\boldsymbol{M}$, $\boldsymbol{C}$ $\boldsymbol{g}$, and $\boldsymbol{\tau}_C$, respectively. The differences between the real parameters and the modeled parameters are referred to as parameter uncertainties. The modeling and compensation of meso-milling cutting force is an ongoing research subject[31] that is beyond the scope of this paper, thus, it is not considered.

Applying feedback linearization, the control law $\boldsymbol{\tau}_{X_E}$ is

$$\boldsymbol{\tau}_{X_E} = \boldsymbol{M}[\ddot{\boldsymbol{x}}_{\text{ref}} + \boldsymbol{u}_{X_E}] + \boldsymbol{C}\dot{\boldsymbol{x}}_E + \boldsymbol{g} + \boldsymbol{\tau}_C, \tag{39}$$

which transforms the system dynamics to a set of linear second-order differential equations, where the controller $\boldsymbol{u}_{X_E}$ can be designed using linear time invariant (LTI) control design methods:[16,18]

$$\begin{cases} \ddot{\boldsymbol{e}} + \boldsymbol{u}_{X_E} = 0 \\ \ddot{\boldsymbol{e}} = \ddot{\boldsymbol{x}}_{\text{ref}} - \ddot{\boldsymbol{x}}_E \end{cases}. \tag{40}$$

From Eq. (36), the following relationship can be obtained:

$$\begin{cases} \dot{\boldsymbol{\varepsilon}} = \boldsymbol{\mathcal{F}}^T\dot{\boldsymbol{e}} + \dot{\boldsymbol{\mathcal{F}}}^T\boldsymbol{e} \\ \ddot{\boldsymbol{\varepsilon}} = \boldsymbol{\mathcal{F}}^T\ddot{\boldsymbol{e}} + 2\dot{\boldsymbol{\mathcal{F}}}^T\dot{\boldsymbol{e}} + \ddot{\boldsymbol{\mathcal{F}}}^T\boldsymbol{e} \end{cases}. \tag{41}$$

In order to satisfy Eq. (42), such that $\boldsymbol{\varepsilon} \to 0$ as $t \to \infty$

$$\ddot{\varepsilon} + \boldsymbol{K}_d\dot{\varepsilon} + \boldsymbol{K}_p\varepsilon = 0. \tag{42}$$

$\boldsymbol{u}_{X_E}$ is defined as

$$u = (\mathcal{F}^T)^{-1}\left(\boldsymbol{K}_d\dot{\varepsilon} + \boldsymbol{K}_p\varepsilon + 2\mathcal{F}^T\dot{e} + \mathcal{F}^T e\right). \tag{43}$$

The linear controller $\boldsymbol{K} = [\boldsymbol{K}_p \ \boldsymbol{K}_d]$ is designed using the convex combination controller design procedure.

3.3. Convex combination controller design method

The notion that certain performance specifications are convex is outlined in ref. [17]. The convex combination controller design methodology was first developed in ref. [18], and the design procedure is outlined below. Since designing a controller to satisfy a single specification is less challenging than attempting to satisfy multiple specifications at once, the convex combination method seeks to design controllers to first satisfy individual convex specifications, and then form the convex combination of these controllers to simultaneously satisfy all specifications. This

https://doi.org/10.1017/S0263574713000842 Published online by Cambridge University Press

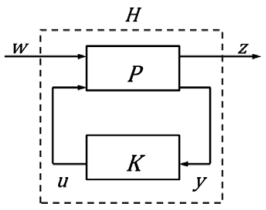

Fig. 3. Uniform framework.

method is applied to the control design of PKMs since it provides an opportunity to define and satisfy multiple closed-loop performance specifications relevant to PKMs explicitly, such as robust performance.

A performance specification, defined as a functional $\varphi(H)$ on a closed-loop system H, is convex if it satisfies the following:

$$\varphi\left(\lambda H_1 + (1-\lambda)\, H_2\right) \leq \lambda\varphi\left(H_1\right) + (1-\lambda)\,\varphi\left(H_2\right), \tag{44}$$

for $\lambda \in [0, 1]$, and two closed-loop systems H_1 and H_2. Satisfactory performance is quantified as

$$\varphi\left(H\right)_k \leq \alpha_k, \tag{45}$$

where α_k is the minimum specification value.[18]

It is assumed that the system plant and the controller are LTI. The closed-loop system is first formulated into the uniform framework, developed in ref. [17], Fig. 3. Note that $\boldsymbol{w}$ is the exogenous input signal, $\boldsymbol{u}$ is the control signal, $\boldsymbol{y}$ is the sensed output and z is the regulated output. The system plant $\boldsymbol{P}$ is expressed as a matrix containing four transfer functions P_{zw}, P_{zu}, P_{yw}, and P_{yu} from parings between the output z, $\boldsymbol{y}$ and input $\boldsymbol{w}$, $\boldsymbol{u}$:

$$\begin{bmatrix} \boldsymbol{z} \\ \boldsymbol{y} \end{bmatrix} = \boldsymbol{P} \begin{bmatrix} \boldsymbol{w} \\ \boldsymbol{u} \end{bmatrix} = \begin{bmatrix} P_{zw} & P_{zu} \\ P_{yw} & P_{yu} \end{bmatrix} \begin{bmatrix} \boldsymbol{w} \\ \boldsymbol{u} \end{bmatrix}. \tag{46}$$

The derivation of the closed-loop system H is presented in ref. [17], shown in Eq. (47):

$$H = P_{zw} + P_{zu}\boldsymbol{K}(I - P_{yu}\boldsymbol{K})^{-1}P_{yw}. \tag{47}$$

An algebraic expression R is defined below in Eq. (48) from selected terms in H, which can be used to perform convex combination:

$$R = \boldsymbol{K}\left(I - P_{yu}\boldsymbol{K}\right)^{-1}. \tag{48}$$

From n performance specifications, the list of minimum satisfactory specification values is

$$\boldsymbol{\Psi} = [\alpha_1 \;\; \alpha_2 \;\; \cdots \;\; \alpha_n]^T. \tag{49}$$

For n performance specifications, sample controllers $\boldsymbol{K}_j$, for $k = 1, 2, \ldots, m$, are designed first using any LTI controller design method (with maximum number n, and $m \leq n$) such that each performance specification is satisfied by at least one sample controller. Then, convex combination can be applied to form a single controller $\boldsymbol{K}^*$ from the set of $\boldsymbol{K}_j$, such that all performance specifications are satisfied simultaneously.

Assuming $m = n$ and that there are n sample controllers forming n number of H_j, the functional $\varphi(H_j)_k$, or φ_{jk} for each α_k can be determined. The result is formulated into a square matrix $\boldsymbol{\varphi}$, defined

https://doi.org/10.1017/S0263574713000842 Published online by Cambridge University Press

Table I. List of closed-loop performance specifications.

	Closed-loop performance specifications		Desired specification value
(DS-1)	Contour position tracking error	$\varphi_{\varepsilon con} = \left\|\varepsilon_n \hat{n} + \varepsilon_b \hat{b}\right\|^2$	$<1 \times 10^{-7}$m
(DS-2)	Lag position tracking error	$\varphi_{\varepsilon lag} = \left\|\varepsilon_t \hat{t}\right\|^2$	$<8 \times 10^{-7}$m
(DS-3)	Contour velocity tracking error	$\varphi_{\varepsilon c\_d} = \left\|\dot{\varepsilon}_n \hat{n} + \dot{\varepsilon}_b \hat{b}\right\|^2$	$<2 \times 10^{-5}$m/s
(DS-4)	Lag velocity tracking error	$\varphi_{\varepsilon l\_d} = \left\|\dot{\varepsilon}_t \hat{t}\right\|^2$	$<1 \times 10^{-4}$m/s
(DS-5)	Task space actuation effort	$\varphi_u = \|u\|^2$	<3.46N
(DS-6)	Robust stability/performance	$\varphi_{\text{ROBUST}} = \delta \|KH\| + \delta_x \|H\|$	< 1.00

as

$$\boldsymbol{\varphi} = \begin{bmatrix} \varphi_{11} & \cdots & \varphi_{1m} \\ \vdots & \ddots & \vdots \\ \varphi_{n1} & \cdots & \varphi_{nm} \end{bmatrix}_{m=n}. \tag{50}$$

Each row of $\boldsymbol{\varphi}$ consists of values of corresponding to performance specification α_k for closed-loop system H_1 to H_m resulting from sample controllers $\boldsymbol{K}_1$ to $\boldsymbol{K}_m$.

The general case of formulation of $\boldsymbol{\varphi}$, when the number of sample controllers is less than the number of performance specifications, is discussed in ref. [32]. If a convex solution exists, a convex combination vector $\boldsymbol{\Lambda}$ can be solved using linear programming.

$$\boldsymbol{\Lambda} = [\,\lambda_1 \quad \lambda_2 \quad \cdots \quad \lambda_n\,]. \tag{51}$$

Two conditions were presented in ref. [32], which must be satisfied in order to have a solution to $\boldsymbol{\Lambda}$. If a solution does not exist, then, new sample controllers must be designed.

Performing convex combination of H_j with $\boldsymbol{\Lambda}$ yields H^* in Eq. (52). However, H shares a one-to-one correspondence to the expression R as shown in Eqs. (47) and (48), thus, the expressions R_j can be used to form R^* in Eq. (52):

$$\begin{cases} H^* = \lambda_1 H_1 + \lambda_2 H_2 + \cdots + \lambda_i H_i \\ R^* = \lambda_1 R_1 + \lambda_2 R_2 + \cdots + \lambda_i R_i \end{cases}. \tag{52}$$

From Eq. (48), the convex combination controller $\boldsymbol{K}^*$ is solved from R^* as

$$\boldsymbol{K}^* = (I + R^* P_{yu})^{-1} R^*. \tag{53}$$

4. Controller Design and Simulations

4.1. Performance specifications

The closed-loop performance specifications under consideration for the PKM-based mMT are the contour and position lag error, the contour and lag velocity tracking error, both developed in Section 3.1. Also considered are the actuation effort and robust performance. Table I lists six closed-loop performance specifications relevant to the position control of the mMT. These specifications are shown to be convex by refs. [17, 18]. The desired specification values are shown in the last column of Table I.

Since the compensation of contour error is more important than lag error, the desired contour error tracking specifications are more stringent than the lag error tracking specifications. The actuation specification places a maximum limit on the magnitude of the control signal to prevent saturation. The robust stability/performance specification $\varphi_{\text{ROBUST}} = \delta_{\mathcal{D}} \|\boldsymbol{K}H\| + \delta_x H$ is proposed by ref. [16]. $\delta_{\mathcal{D}}$ is a measure of the parameter variation on the mass matrix, modeled as multiplicative uncertainties.

https://doi.org/10.1017/S0263574713000842 Published online by Cambridge University Press

Table II. Sample controller designs.

Controller 1	$\boldsymbol{K}_1 = \begin{bmatrix} 2e6 & 0 & 0 & 1e4 & 0 & 0 \\ 0 & 10e6 & 0 & 0 & 5e4 & 0 \\ 0 & 0 & 10e6 & 0 & 0 & 5e4 \end{bmatrix}$
Controller 2	$\boldsymbol{K}_2 = \begin{bmatrix} 1.5e6 & 0 & 0 & 0.8e4 & 0 & 0 \\ 0 & 11e6 & 0 & 0 & 5.5e4 & 0 \\ 0 & 0 & 11e6 & 0 & 0 & 5.5e4 \end{bmatrix}$
Controller 3	$\boldsymbol{K}_3 = \begin{bmatrix} 1.2e6 & 0 & 0 & 0.5e4 & 0 & 0 \\ 0 & 9e6 & 0 & 0 & 4e4 & 0 \\ 0 & 0 & 9e6 & 0 & 0 & 4e4 \end{bmatrix}$
Controller 4	$\boldsymbol{K}_4 = \begin{bmatrix} 0.1e6 & 0 & 0 & 0.2e4 & 0 & 0 \\ 0 & 15e6 & 0 & 0 & 5.5e4 & 0 \\ 0 & 0 & 15e6 & 0 & 0 & 5.5e4 \end{bmatrix}$
Controller 5	$\boldsymbol{K}_5 = \begin{bmatrix} 5e6 & 0 & 0 & 1.2e4 & 0 & 0 \\ 0 & 8e6 & 0 & 0 & 5e4 & 0 \\ 0 & 0 & 8e6 & 0 & 0 & 5e4 \end{bmatrix}$

Table III. Closed-loop performance specification values and controller performances.

	φ_u	φ_{ROBUST}	$\varphi_{\varepsilon\text{con}}$	$\varphi_{\varepsilon c\_d}$	$\varphi_{\varepsilon\text{lag}}$	$\varphi_{\varepsilon l\_d}$
$\boldsymbol{\Psi}$	<3.46	<1.00	$<1 \times 10^{-7}$	$<2 \times 10^{-5}$	$<8 \times 10^{-7}$	$<1 \times 10^{-4}$
$\boldsymbol{K}_1$	3.461	**0.9489**	1.00×10^{-7}	2.00×10^{-5}	$\mathbf{5.00 \times 10^{-7}}$	1.00×10^{-4}
$\boldsymbol{K}_2$	3.468	**0.9827**	$\mathbf{0.907 \times 10^{-7}}$	$\mathbf{1.82 \times 10^{-5}}$	$\mathbf{6.68 \times 10^{-7}}$	1.26×10^{-4}
K_3	**3.456**	**0.8391**	1.11×10^{-7}	2.51×10^{-5}	8.31×10^{-7}	1.99×10^{-4}
$\boldsymbol{K}_4$	3.522	**0.9654**	$\mathbf{0.70 \times 10^{-7}}$	$\mathbf{1.82 \times 10^{-5}}$	$\mathbf{0.997 \times 10^{-7}}$	5.01×10^{-4}
$\boldsymbol{K}_5$	**3.408**	**0.9575**	1.25×10^{-7}	2.00×10^{-5}	$\mathbf{2.00 \times 10^{-7}}$	0.83×10^{-4}
$\boldsymbol{K}^*$	**3.4521**	**0.9750**	$\mathbf{0.964 \times 10^{-7}}$	$\mathbf{1.91 \times 10^{-5}}$	$\mathbf{5.49 \times 10^{-7}}$	$\mathbf{0.88 \times 10^{-4}}$

It forms a trade-off with the size of the linear controller $\boldsymbol{K}$in $\|KH\|$, which determines the actuator stiffness against external disturbances. δ_x is the allowable parameter variation for C and G.

4.2. Controller design

The sample controllers $\boldsymbol{K}_j$ can be designed using any linear control design method such that each sample controller satisfies at least one closed-loop performance specification. The sample controllers, as shown in Table II, are designed using the linear-quadratic regulator (LQR) method such that the compensation for contour error (row 2 and 3 of $\boldsymbol{K}_j$) is weighted significantly more than the lag errors (row 1 of $\boldsymbol{K}_j$). Since contour error compensation is more important, giving it higher weighting in control command relative to lag error compensation leads to better machining tracking accuracy. Since all controllers must satisfy robust stability, only five sample controllers are needed. The performances of the controllers with respect to the performance specifications are shown in Table III, where bold font indicates the value meets specification.

The convex combination vector $\boldsymbol{\Lambda}$ is computed as

$$\boldsymbol{\Lambda} = [\,0.012 \quad 0.3489 \quad 0.0062 \quad 0 \quad 0.6329 \quad 0\,]^T. \tag{54}$$

The convex combination controller $\boldsymbol{K}^*$ is solved as

$$\boldsymbol{K}^* = \begin{bmatrix} 1.821e6 & 0 & 0 & 1.136e4 & 0 & 0 \\ 0 & 10.34e6 & 0 & 0 & 5.25e4 & 0 \\ 0 & 0 & 10.34e6 & 0 & 0 & 5.25e4 \end{bmatrix}. \tag{55}$$

https://doi.org/10.1017/S0263574713000842 Published online by Cambridge University Press

Table IV. mMT simulation parameters.

Parameter name	Values
Mass of circular prismatic actuator	0.35 kg
Mass of vertical prismatic actuator	0.35 kg
Mass of vertical guide rail	0.30 kg
Mass of platform	0.0267 kg
Radius of platform	10 mm
Thickness of platform	4 mm
Mass of spindle rotor	0.0073 kg
Radius of spindle rotor	5 mm
Length of tool	10 mm
Mass of link l_{3i}	0.30 kg
Radius of link l_{3i}	5 mm
Length of link l_{3i}	0.150 m
Radius of PKM circular base	0.125 m

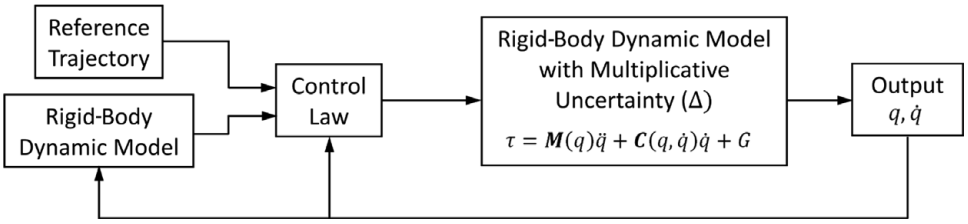

Fig. 4. Simulation block diagram.

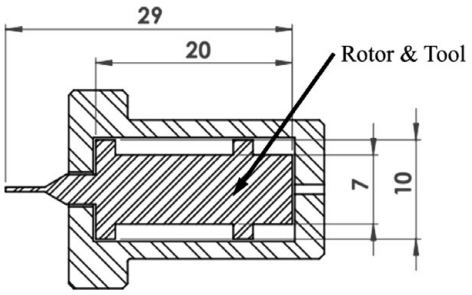

Fig. 5. Micro-spindle simulation model.

The closed-loop performance of $\boldsymbol{K}^*$ can be noted in the last row of Table III to satisfy all six performance specifications.

4.3. Simulations

The dynamic simulation of the PKM-based mMT was implemented in MATLAB Simulink. Experiments were not conducted since issues such as flexible-body analysis and vibration compensation, which affects the motion of the PKM, are not considered in the proposed rigid-body control design. On the other hand, simulations are suitable to validate the design methodology since the control issues under consideration can be isolated. The block diagram of the simulation is shown in Fig. 4, and the dynamic parameters for the proposed mMT are given in Table IV. The simulation for one iteration of the computation of the dynamic model, including the matrices $\boldsymbol{M}$ and $\boldsymbol{C}$, vector $\boldsymbol{g}$, and the Jacobians $\boldsymbol{J}$ and $\boldsymbol{J}^{-1}$ using MATLAB Simulink is about 1.27 ms. The majority of the computation time, 0.88 ms, is used to compute the Jacobians, using derived analytical expressions. The simulations were performed in a MS-Windows operating system-based PC using the Intel Core i7-3770 Processor, which typically is not representative of the processing environment used in industrial PCs.

https://doi.org/10.1017/S0263574713000842 Published online by Cambridge University Press

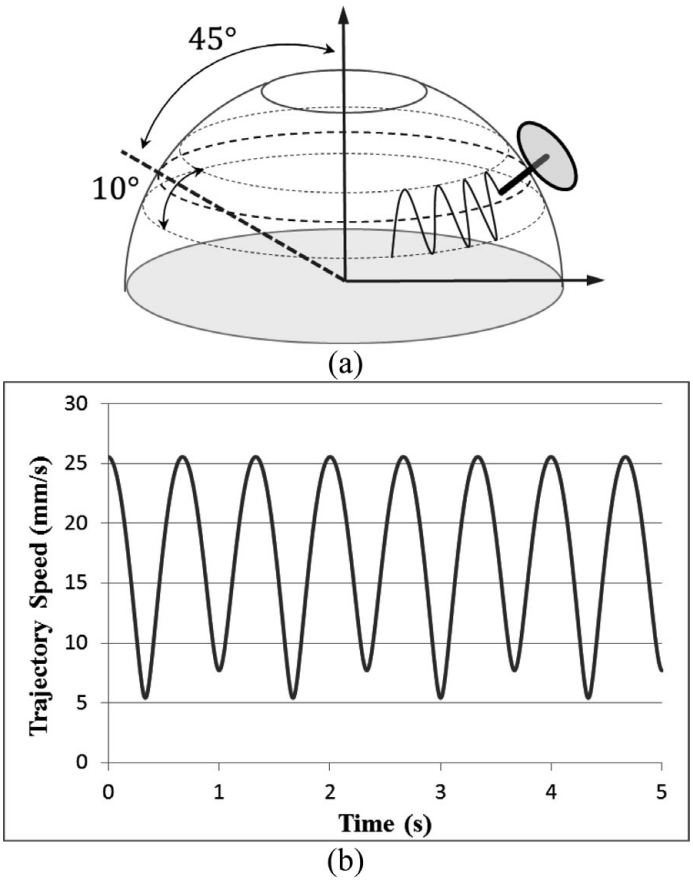

Fig. 6. (a) Simulated tool trajectory; (b) Trajectory speed.

The gyroscopic forces induced by the mMT are simulated within MATLAB, based on a representative micro spindle design shown in Fig. 5. The spindle housing is designed to the scale of the mMT platform and forms a part of the platform structure. The simulations are performed under the assumption that the spindle rotation speed is constant, namely, $\ddot{\xi} = 0$ and $\ddot{\zeta} = \ddot{\gamma}$.

The reference trajectory of the mMT is a combination of circular and sinusoidal motion imposed on a 30-mm hemispherical workspace, Fig. 6(a). The range of feed rate for meso-milling is typically between 0.5 μm/flute and 3.0 μm/flute.[31] Converting the feed rate (μm/flute) to cutting speed (mm/s) based on a two-flute tool and a maximum spindle speed of 250,000 rpm yields a cutting speed range between 4.17 mm/s and 25.00 mm/s. As can be noted from Fig. 6(b), the simulation trajectory covers this range. The expressions for the reference paths are shown in Eqs. (56) and (57):

$$\begin{cases} x_{\text{ref}} = R_{ws}\cos(\sigma)\cos(\omega) \\ y_{\text{ref}} = R_{ws}\cos(\sigma)\sin(\omega) \\ z_{\text{ref}} = -0.08 + R_{ws}\sin(\sigma) \\ \alpha_{\text{ref}} = \omega \\ \beta_{\text{ref}} = -\sigma + {}^{\pi}/_{2} \\ \gamma_{\text{ref}} = 0 \end{cases}, \tag{56}$$

where

$$\begin{cases} \sigma = \frac{\pi}{4} + \frac{\pi}{18}\cdot\sin(1.5\pi\cdot t), \\ \omega = 0.1\pi\cdot t, \\ R_{ws} = 0.030 \text{ m}. \end{cases} \tag{57}$$

https://doi.org/10.1017/S0263574713000842 Published online by Cambridge University Press

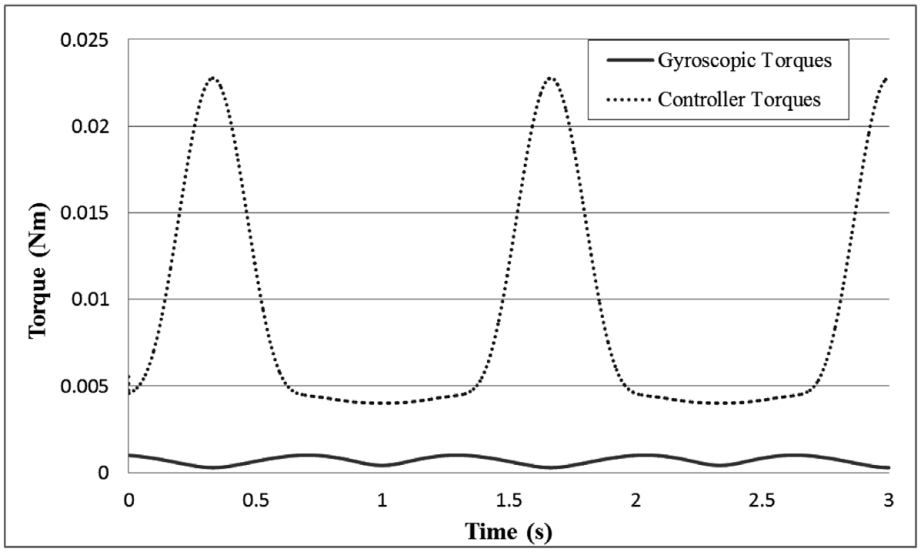

Fig. 7. Gyroscopic torque magnitude vs. controller torque output.

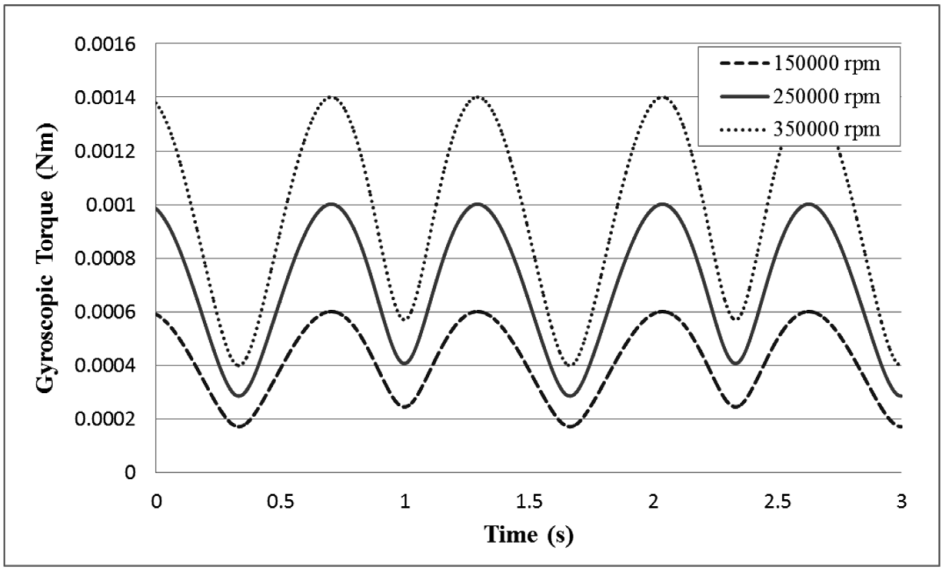

Fig. 8. Effect of spindle mass and speed on gyroscopic forces.

The maximum magnitude of the gyroscopic torques is found to be 5% of the magnitude of the Euler angle control torques, Fig. 7. For high-precision applications, such as for the mMT, the contribution of this gyroscopic force to tracking errors cannot be neglected and must be compensated. This is evident when system robustness is taken into account, where it is desirable to reduce the value of un-modeled distance forces such that margin for the allowable system parameter variations is increased. Figure 8 shows the variation of tracking error when the spindle is rotating at different speeds. The relationship between the two variables is proportional.

The actual contour error can be determined using a search algorithm implemented during MATLAB simulation by finding the vector with the shortest magnitude between the reference tool path and the current tool location. The contour error estimates from the circular approximation method are then compared against this true contour error to determine its performance as shown in Fig. 9. The radius of curvature of this trajectory reaches a minimum of 200 μm. As expected, the performance of contour

https://doi.org/10.1017/S0263574713000842 Published online by Cambridge University Press

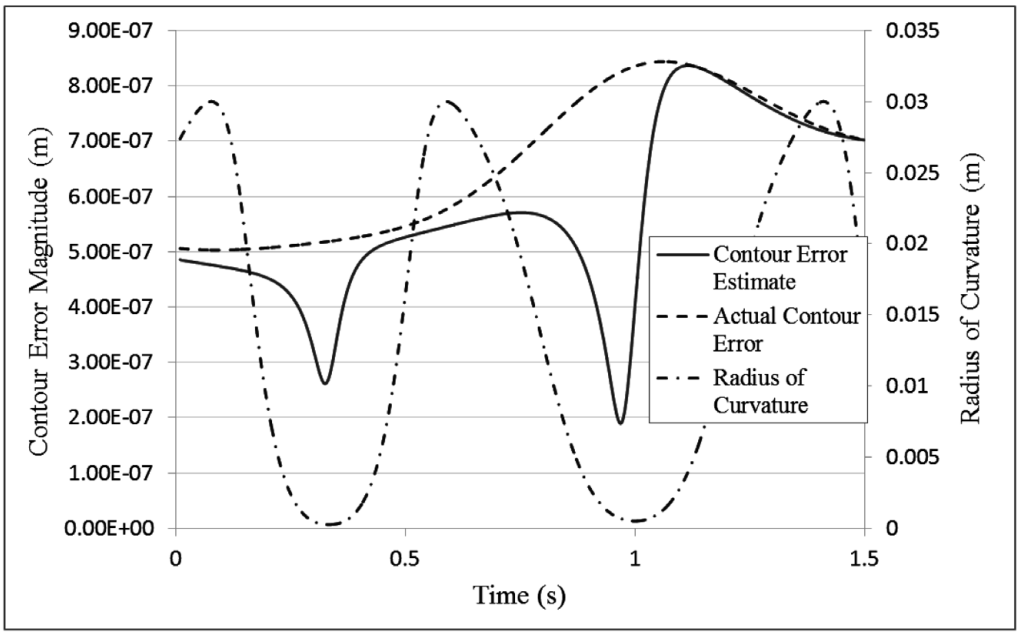

Fig. 9. Actual contour error vs. circular approximation.

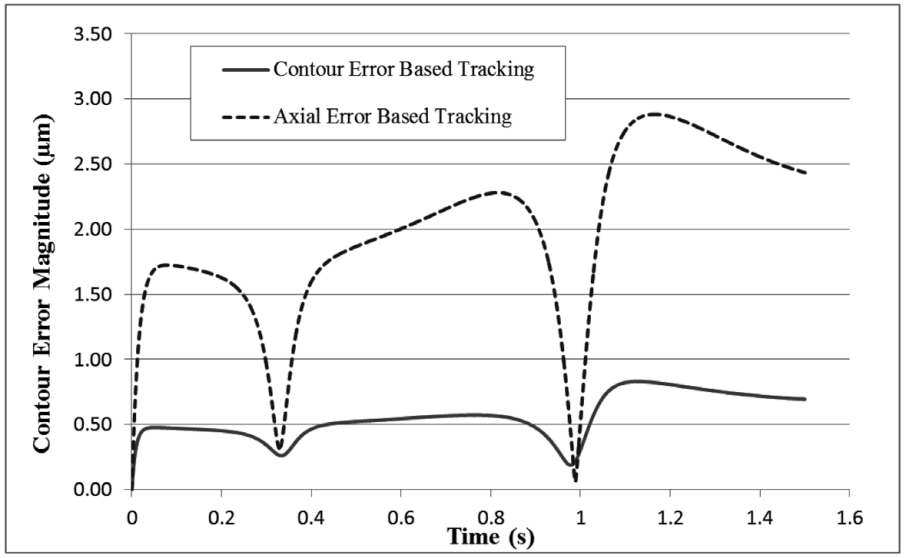

Fig. 10. Control performance using contour/lag error tracking vs. axial error tracking.

error estimation in proximity of this minimum tends to be worse and the value of the estimation is less than the actual contour error.

In Fig. 10, the control performance using contour/lag error-based tracking versus axial error-based tracking can be compared. The contour error can be evaluated for both control implementations. In the contour/lag error-based tracking, the contour error is compensated directly in the control law. In order to make a meaningful comparison, the norms of the controllers $\boldsymbol{K}$ in both control implementations are set to be the same. In the axial-based error, the contour error is computed but not implemented in the control algorithm. It is shown in Fig. 10 that the control implementation using contour/lag-based tracking error yields better tracking performance since the resulting contour error is less than using axial error-based control.

https://doi.org/10.1017/S0263574713000842 Published online by Cambridge University Press

Table V. Controller design with adjusted weight for contour error compensation.

Controller 1	$\boldsymbol{K}_{p1} = \begin{bmatrix} 1e6 & 0 & 0 \\ 0 & 1e6 & 0 \\ 0 & 0 & 1e6 \end{bmatrix}$	$\left\|\boldsymbol{K}_{p1}\right\|_F = 1.732e6$
	$\boldsymbol{K}_{d1} = \begin{bmatrix} 9e3 & 0 & 0 \\ 0 & 9e3 & 0 \\ 0 & 0 & 9e3 \end{bmatrix}$	$\|\boldsymbol{K}_{d1}\|_F = 1.559e4$
Controller 2		$\left\|\boldsymbol{K}_{p2}\right\|_F = 1.734e6$
	$\boldsymbol{K}_{d2} = \begin{bmatrix} 6.5e3 & 0 & 0 \\ 0 & 10e3 & 0 \\ 0 & 0 & 10e3 \end{bmatrix}$	$\|\boldsymbol{K}_{d2}\|_F = 1.556e4$
Controller 3	$\boldsymbol{K}_{p3} = \begin{bmatrix} 0.3e6 & 0 & 0 \\ 0 & 1.21e6 & 0 \\ 0 & 0 & 1.21e6 \end{bmatrix}$	$\|\boldsymbol{K}_{p3}\|_F = 1.737e6$
	$\boldsymbol{K}_{d3} = \begin{bmatrix} 4.5e3 & 0 & 0 \\ 0 & 10.5e3 & 0 \\ 0 & 0 & 10.5e3 \end{bmatrix}$	$\|\boldsymbol{K}_{d3}\|_F = 1.552e4$

In axial control, the control gains in the diagonal elements of $\boldsymbol{K}_p$ and $\boldsymbol{K}_d$ must be the same to provide equal control effort along the three axes. Within the contour/lag control framework, it is clear that Elements (2,2) and (3,3) of $\boldsymbol{K}_p$ and $\boldsymbol{K}_d$ are for the control of contour error while Element (1,1) is for the control of lag error. Thus, it is possible to adjust the weighting of these elements to place more emphasis on contour error control at the expense of lag error performance without increasing the overall Frobenius norm of $\boldsymbol{K}_p$ and $\boldsymbol{K}_d$ matrices.

In Table V, three different sample controllers are devised and simulated to illustrate this concept. From controllers 1 to 3, Element (1,1) of $\boldsymbol{K}_p$ and $\boldsymbol{K}_d$ decreases while the other two diagonal elements increase. The difference in Frobenius norms of these three controllers is within 1%.

From Fig. 11(a), it is noted that the contour error is decreased by approximately 20% from controllers 1 to 3. At the same time, the lag error in Fig. 11(b) is increased by approximately 300% from controllers 1 to 3. This is expected since to increase the gains for Elements (2,2) and (3,3), a substantial decrease must happen for Element (1,1) in order to maintain the same matrix norm. However, for this simulation, the magnitude of the lag error for controller 3 is smaller than the corresponding contour error. It is entirely possible that the lag error may exceed 0.1 μm without significantly impacting the control performance because the contour error would be further minimized. A large lag error will only be problematic if the radius of curvature of the trajectory tool path is decreased by a significant margin such that the contour error estimation is no longer accurate.

5. Conclusions

In order to address multiple control issues in the design of PKMs, a novel methodology for the dynamic modeling and control of PKMs is presented. In order to address the issue of synchronous control for PKMs, a novel contour error formulation based on circular approximation is presented. The approximation is completely geometric and does not rely on time delay estimations. Since contour error is more significant for machining accuracy, it is shown that by increasing the weighting of contour error compensation at the cost of a larger lag error, the overall machining accuracy is significantly improved. A robust performance specification is formulated separately based on the linear-multivariable approach and the convex combination controller design methodology is applied to address the issue of satisfying multiple closed-loop performance specifications, including both contour error and robust performance, simultaneously. The methodology is applied to a desktop PKM-based mMT for five-axis meso-milling operations. The dynamic model of mMT spindle is developed and the gyroscopic torques can be up to 5% of the actuation torques, which is a significant disturbance force and must be compensated directly.

https://doi.org/10.1017/S0263574713000842 Published online by Cambridge University Press

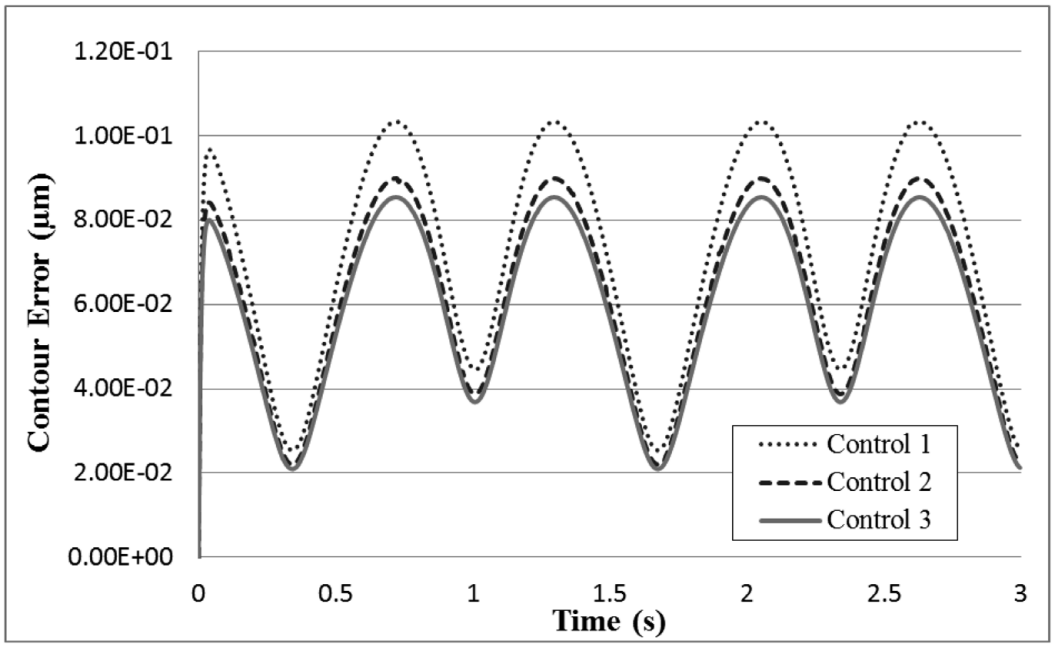

(a)

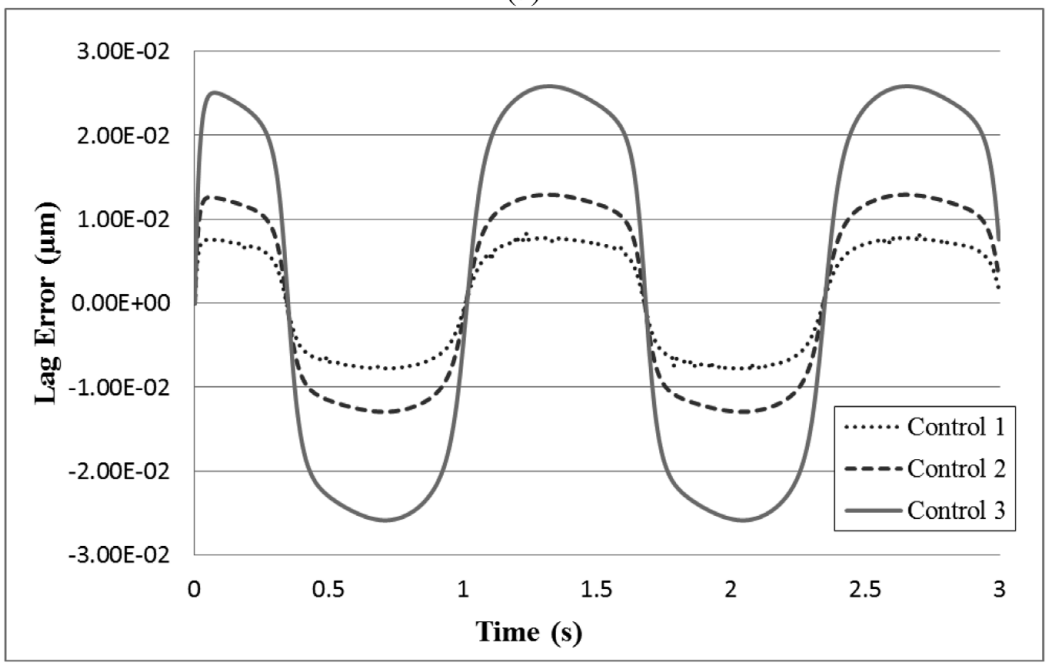

(b)

Fig. 11. Improvement in contour error compensation with weighted control gains. (a) Contour error with varying control gains; (b) Lag error with varying control gains.

Acknowledgements

The authors thank the NSERC Canadian Network for Research and Innovation in Machining Technology (CANRIMT) for funding this research project.

References

1. M. P. Vogler, X. Liu, S. G. Kapoor, R. E. DeVor and K. F. Ehmann, "Development of meso-scale machine tool (mMT) systems," Technical Paper, Society of Manufacturing Engineers MS.MS02-181, 1–9, (2002).
2. Y.-B. Bang, K.-M. Lee and S. Oh, "5-axis micro milling machine for machining micro parts," *Int. J. Adv. Manuf. Technol*. **25**(9–10), 888–894 (2005).

https://doi.org/10.1017/S0263574713000842 Published online by Cambridge University Press

3. E. Kussul, T. Baidyk, L. Ruiz-Huerta, A. Caballero-Ruiz, G. Velasco and L. Kasatkina, "Development of micromachine tool prototypes for microfactories," *J. Micromech. Microeng.* **12**(6), 795–812 (2002).
4. H. Azulay, C. Hawryluck, J. K. Mills and B. Benhabib, "Configuration Design of a Meso-Milling machine," *Proceedings of the 23rd Canadian Congress of Applied Mechanics*, Vancouver, Canada (2011) pp. 1024–1027.
5. B. Dasgupta and T. Mruthyunjaya, "A Newton-Euler formulation for the inverse dynamics of the Stewart platform manipulator," *Mech. Mach. Theory* **33**(8), 1135–1152 (1998).
6. L.-W. Tsai, "Solving the inverse dynamics of a Stewart-Gough manipulator by the principle of virtual work," *Trans ASME, J. Mech. Des.* **122**(1), 3–9 (2000).
7. H. Abdellatif and B. Heimann, "Computational efficient inverse dynamics of 6-DOF fully parallel manipulators by using the Lagrangian formalism," *Mech. Mach. Theory* **44**(1), 192–207 (2009).
8. G. Liu, X. Wu and Z. Li, "Inertia Equivalence Principle and Adaptive Control of Redundant Parallel Manipulators," *Proceedings of the 2002 IEEE International Conference on Robotics and Automation*, Washington DC, USA (2002) pp. 835–840.
9. S. Weiwei, C. Shuang, Z. Yaoxin and L. Yanyang, "Active joint synchronization control for a 2-DOF redundantly actuated parallel manipulator," *IEEE Trans. Control Syst. Technol*. **17**(2), 416–423 (2009).
10. Y. Koren, "Cross-coupled biaxial computer control for manufacturing systems," *Trans. ASME, J. Dyn. Syst. Meas. Control* **102**(4), 265–272, (1980).
11. Y. Koren and C.-C. Lo, "Variable-gain cross-coupling controller for contouring," *CIRP Ann.–Manuf. Technol*. **40**(1), 371–374 (1991).
12. G.-C. Chiu and M. Tomizuka, "Contouring control of machine tool feed drive systems: A task coordinate frame approach," *IEEE Trans. Control Syst. Technol*. **9**(1), 130–139 (2001).
13. B. Sencer, Y. Altintas and E. Croft, "Modeling and control of contouring errors for five-axis machine tools–Part I: Modeling," *Trans ASME*, *J. Manuf. Sci. Eng.* **131**(3), 0310061–0310068 (2009).
14. A. El Khalick M and N. Uchiyama, "Contouring controller design based on iterative contour error estimation for three-dimensional machining," *Robot. Comput.-Integr. Manuf.* **27**(4), 802–807 (2011).
15. J. Yang and Z. Li, "A novel contour error estimation for position loop-based cross-coupled control," *IEEE/ASME Trans. Mechatronics* **16**(4), 643–655 (2011).
16. M. W. Spong and M. Vidyasagar, "Robust linear compensator design for nonlinear robotic control," *IEEE J. Robot. Autom.* **3**(4), 345–351 (1987).
17. S. P. Boyd and C. H. Barratt, *Linear Controller Design: Limits of Performance* (Prentice Hall, Englewood Cliffs, NJ, 1991).
18. H. H. Liu and J. K. Mills, "Robot trajectory control system design for multiple simultaneous specifications: Theory and experimentation," *Trans. ASME, J. Dyn. Syst., Meas. Control* **120**(4), 520–523 (1998).
19. A. E. Honegger, G. Q. Langstaff, A. G. Phillip and T. D. Vanravenswaay, "Development of an automated microfactory: Part 1–microfactory architecture and sub-systems development," *Trans. North Am. Manuf. Res. Inst. SME* **34**, 341–348 (2006).
20. S. Jahanmir, Z. Ren, H. Heshmat and M. Tomaszewski, "Design and evaluation of an ultrahigh speed micro-machining spindle," *Mach. Sci. Technol.* **14**(2), 224–243 (2010).
21. M. Mahmoodi, Y. Le, J. K. Mills and B. Benhabib, "An Active Dynamic Model for a Parallel-Mechanism-Based Meso-Milling Machine Tool," *Proceedings of the 23rd Canadian Congress of Applied Mechanics*, Vancouver, Canada (2011) pp. 1032–1035.
22. M. Mahmoodi, J. Mills and B. Benhabib, "Structural Vibration Modeling of a Novel Parallel Mechanism-Based Reconfigurable Meso-Milling Machine Tool (RmMT)," *Proceedings of the 1st International Conference on Virtual Machining Process Technology*, Montreal, Canada (2012).
23. Y. Le, J. Mills and B. Benhabib, "Convex Combination Control Design for 6 DOF Spatial Reconfigurable Meso-Milling Machine Tool," *Proceedings of the 1st International Conference on Virtual Machining Process Technology*, Montreal, Canada (2012).
24. J. Kim, K. Cho, J. Hwang, C. Iurascu and F. Park, "Eclipse-RP: A new RP machine based on repeated deposition and machining," *Proc. Inst. Mech. Eng.* **216**(K1), 13–20 (2002).
25. Y. Li and Q. Xu, "Kinematics and inverse dynamics analysis for a general 3-PRS spatial parallel mechanism," *Robotica* **23**(2), 219–229 (2005).
26. C.-T. Chen, "A Lagrangian formulation in terms of quasi-coordinates for the inverse dynamics of the general 6–6 Stewart platform manipulator," *JSME Int. J.* C **46**(3), 1084–1090 (2003).
27. J. Kim and F. C. Park, "Direct kinematic analysis of 3-RS parallel mechanisms," *Mech. Mach. Theory* **36**(10), 1121–1134 (2001).
28. L. Sciavicco and B. Siciliano, *Modeling and Control of Robot Manipulators* (The McGraw-Hill Companies, Inc., New York, N. Y., 1996).
29. E. Kreyszig, *Differential Geometry* (University of Toronto Press, Toronto, 1959).
30. C. Abdallah, D. Dawson, P. Dorato and M. Jamshidi, "Survey of robust control for rigid robots," *IEEE Control Syst.* **11**(2), 24–30 (1991).
31. J. Miao, G. Chen, X. Lai, H. Li and C. Li, "Review of dynamic issues in micro-end-milling," *Int. J. Adv. Manuf. Technol*. **31**(9–10), 897–904 (2007).
32. K. Fu and J. K. Mills, "A convex approach solving simultaneous mechanical structure and control system design problems with multiple closed-loop performance specifications," *Trans. ASME* G **127**(1), 57–68 (2005).